

Chiral singlet superconductivity in the weakly correlated metal LaPt₃P

P. K. Biswas,^{1,*} S. K. Ghosh,^{2,†} J. Z. Zhao,³ D. A. Mayoh,⁴ N. D. Zhigadlo,^{5,6}
Xiaofeng Xu,⁷ C. Baines,⁸ A. D. Hillier,¹ G. Balakrishnan,⁴ and M. R. Lees⁴

¹ISIS Pulsed Neutron and Muon Source, STFC Rutherford Appleton Laboratory,
Harwell Campus, Didcot, Oxfordshire OX11 0QX, United Kingdom

²School of Physical Sciences, University of Kent, Canterbury CT2 7NH, United Kingdom

³Co-Innovation Center for New Energetic Materials,
Southwest University of Science and Technology, Mianyang, 621010, China

⁴Physics Department, University of Warwick, Coventry, CV4 7AL, United Kingdom

⁵Laboratory for Solid State Physics, ETH Zurich, 8093 Zurich, Switzerland

⁶CrystMat Company, 8037 Zurich, Switzerland

⁷Department of Applied Physics, Zhejiang University of Technology, Hangzhou 310023, China

⁸Laboratory for Muon Spin Spectroscopy, Paul Scherrer Institute, CH-5232 Villigen PSI, Switzerland

(Dated: January 26, 2021)

Topological superconductors (SCs) are novel phases of matter with nontrivial bulk topology. They host at their boundaries and vortex cores zero-energy Majorana bound states, potentially useful in fault-tolerant quantum computation [1]. Chiral SCs [2] are particular examples of topological SCs with finite angular momentum Cooper pairs circulating around a unique chiral axis, thus spontaneously breaking time-reversal symmetry (TRS). They are rather scarce and usually feature triplet pairing: best studied examples in bulk materials are UPt₃ and Sr₂RuO₄ proposed to be *f*-wave and *p*-wave SCs respectively, although many open questions still remain [2]. Chiral triplet SCs are, however, topologically fragile with the gapless Majorana modes weakly protected against symmetry preserving perturbations in contrast to chiral singlet SCs [3, 4]. Using muon spin relaxation (μ SR) measurements, here we report that the weakly correlated pnictide compound LaPt₃P has the two key features of a chiral SC: spontaneous magnetic fields inside the superconducting state indicating broken TRS and low temperature linear behaviour in the superfluid density indicating line nodes in the order parameter. Using symmetry analysis, first principles band structure calculation and mean-field theory, we unambiguously establish that the superconducting ground state of LaPt₃P is chiral *d*-wave singlet.

Cooper pairs in conventional SCs, such as the elemental metals, form due to pairing of electrons by phonon-mediated attractive interaction into the most symmetric *s*-wave spin-singlet state [5]. In contrast, unconventional SCs defined as having zero average onsite pairing amplitude pose a pivotal challenge in resolving how superconductivity emerges from a complex normal state. They usually require a long-range interaction [6] and have lower symmetry Cooper pairs. A special class of unconventional SCs are the chiral SCs. A well established realization of a chiral *p*-wave triplet state is the *A*-phase of

superfluid He³ [7]. In addition to UPt₃ and Sr₂RuO₄, the heavy fermion SC UTe₂ is also proposed to be a chiral triplet SC [8]. The chiral singlet SCs are, however, extremely rare and are proposed to be realized within the hidden order phase of the strongly correlated heavy fermion SC URu₂Si₂ [9] and in the locally noncentrosymmetric material SrPtAs [10] with many unresolved issues.

LaPt₃P is a member of the platinum pnictide family of SCs APt₃P (*A* = Ca, Sr and La) with a centrosymmetric primitive tetragonal structure [11]. Its $T_c = 1.1$ K is significantly lower than its other two isostructural counterparts SrPt₃P ($T_c = 8.4$ K) and CaPt₃P ($T_c = 6.6$ K) [11] which are conventional Bardeen-Cooper-Schrieffer (BCS) SCs. Indications of the unconventional nature of superconductivity in LaPt₃P come both from theory: first principles Migdal-Eliashberg-theory [12] and experiments: very low T_c , unsaturated resistivity up to room temperature and a weak specific heat jump at T_c [11]. The chiral nature of superconductivity of LaPt₃P with topologically protected Majorana Fermi-arc and Majorana flat-band, which we uncover here, fits nicely with these characteristics.

Experimental results

We have performed a comprehensive analysis of the superconducting properties of LaPt₃P using the μ SR technique. Two sets of polycrystalline LaPt₃P specimens, referred to here as sample-A (from Warwick, UK) and sample-B (from ETH, Switzerland), were synthesized at two different laboratories by completely different methods. Zero-field (ZF), longitudinal-field (LF), and transverse-field (TF) μ SR measurements were performed on these samples at two different muon facilities: sample-A in the MUSR spectrometer at the ISIS Pulsed Neutron and Muon Source, UK, and sample-B in the LTF spectrometer at the Paul Scherrer Institut (PSI), Switzerland.

ZF- μ SR measurements reveal spontaneous magnetic fields arising just below $T_c \approx 1.1$ K (example characterization is shown by the zero-field-cooled magnetic susceptibility (χ) data for sample-B on the right axis of Fig. 1b)

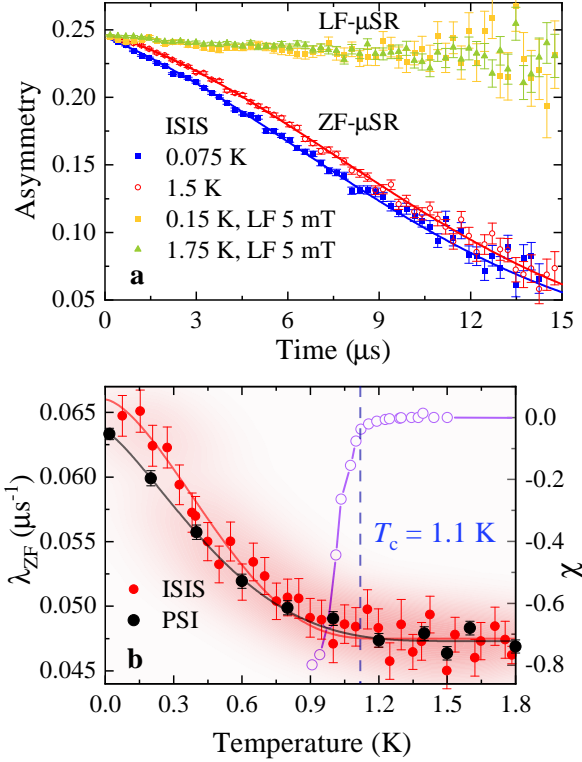


FIG. 1. **Evidence of TRS-breaking superconductivity in LaPt₃P by ZF- μ SR measurements.** **a)** ZF- μ SR time spectra collected at 75 mK and 1.5 K for sample-A of LaPt₃P. The solid lines are the fits to the data using Eq. 1. **b)** The temperature dependence of the extracted λ_{ZF} (left axis) for sample-A (ISIS) and sample-B (PSI) showing a clear increase in the muon spin relaxation rate below T_c . The PSI data has been shifted by $0.004 \mu\text{s}^{-1}$ to match the baseline value of the ISIS data. Variation of the zero-field-cooled magnetic susceptibility (χ) on the right axis for sample-B.

associated with a TRS breaking superconducting state in both samples of LaPt₃P, performed on different instruments. Fig. 1a shows representative ZF- μ SR time spectra of LaPt₃P collected at 75 mK (superconducting state) and at 1.5 K (normal state) on sample-A at ISIS. The data below T_c show a clear increase in muon-spin relaxation rate compared to the data collected in the normal state. To unravel the origin of the spontaneous magnetism at low temperature, we collected ZF- μ SR time spectra over a range of temperatures across T_c and extracted temperature dependence of the muon-spin relaxation rate by fitting the data with a Gaussian Kubo-Toyabe relaxation function $\mathcal{G}(t)$ [13] multiplied by an exponential decay:

$$A(t) = A(0)\mathcal{G}(t)\exp(-\lambda_{ZF}t) + A_{bg} \quad (1)$$

where, $A(0)$ and A_{bg} are the initial and background asymmetries of the ZF- μ SR time spectra, respectively. $\mathcal{G}(t) = \frac{1}{3} + \frac{2}{3}(1 - \sigma_{ZF}^2 t^2) \exp(-\sigma_{ZF}^2 t^2/2)$. σ_{ZF} and λ_{ZF} represent the muon spin relaxation rates originating from

the presence of nuclear and electronic moments in the sample, respectively. In the fitting, σ_{ZF} is found to be nearly temperature independent and hence fixed to the average value of $0.071(4) \mu\text{s}^{-1}$ for sample-A and $0.050(3) \mu\text{s}^{-1}$ for sample-B. The temperature dependence of λ_{ZF} is shown in Fig. 1b. λ_{ZF} has a distinct systematic increase below T_c for both the samples which implies that the effect is sample and spectrometer independent. Moreover, the effect can be suppressed very easily by a weak longitudinal field of 5 mT for both the samples. It is shown in Fig. 1a for sample-A. This strongly suggests that the additional relaxation below T_c is not due to rapidly fluctuating fields [14], but rather associated with very weak fields which are static or quasi-static on the time-scale of muon life-time. The spontaneous static magnetic field arising just below T_c is so intimately connected with superconductivity that we can safely say its existence is direct evidence for TRS-breaking superconducting state in LaPt₃P. From the change $\Delta\lambda_{ZF} = \lambda_{ZF}(T \approx 0) - \lambda_{ZF}(T > T_c)$ we can estimate the corresponding spontaneous internal magnetic field at the muon site $B_{int} \approx \Delta\lambda_{ZF}/\gamma_\mu = 0.22(4)$ G for sample-A and $0.18(2)$ G for sample-B which are very similar to that of other TRS breaking SCs [15]. Here, $\gamma_\mu/(2\pi) = 13.55$ kHz/G is the muon gyromagnetic ratio.

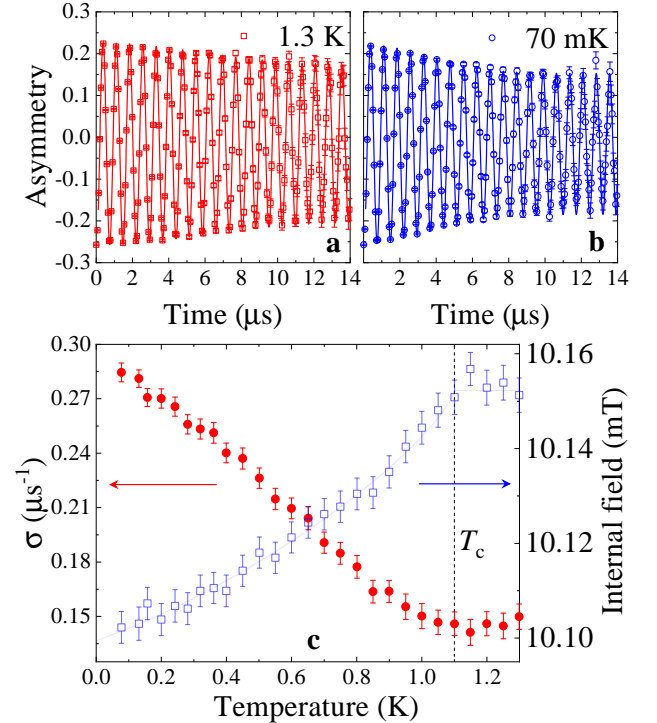


FIG. 2. **Superconducting properties of LaPt₃P by TF- μ SR measurements.** TF- μ SR time spectra of LaPt₃P collected at **a)** 1.3 K and **b)** 70 mK for sample-A in a transverse field of 10 mT. The solid lines are the fits to the data using Eq. 2. **c)** The temperature dependence of the extracted σ (left panel) and internal field (right panel) of sample-A.

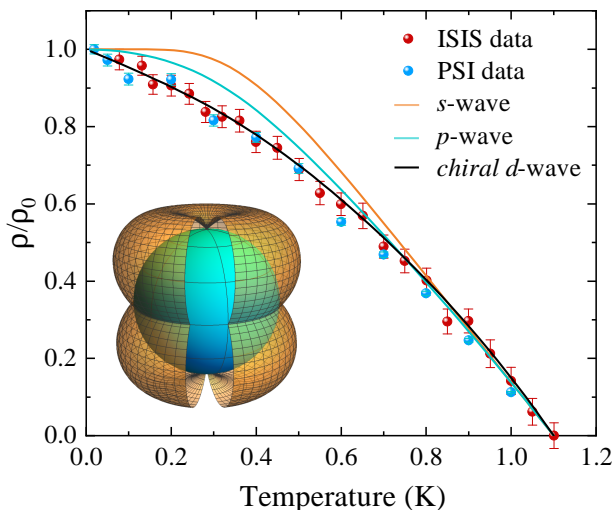


FIG. 3. **Evidence of *chiral d-wave* superconductivity in LaPt₃P.** Superfluid density (ρ) of LaPt₃P as a function of temperature normalized by its zero-temperature value ρ_0 . The solid lines are fits to the data using different models of gap symmetry. Inset shows the schematic representation of the nodes of the *chiral d-wave* state.

We show the TF- μ SR time spectra for sample-A in Fig. 2a and Fig. 2b at two different temperatures. The spectrum in Fig. 2a shows only weak relaxation mainly due to the transverse (2/3) component of the weak nuclear moments present in the material in the normal state at 1.3 K. In contrast, the spectrum in Fig. 2b in the superconducting state at 70 mK shows higher relaxation due to the additional inhomogeneous field distribution of the vortex lattice, formed in the superconducting mixed state of LaPt₃P. The spectra are analyzed using the Gaussian damped spin precession function [13]:

$$A_{TF}(t) = A(0) \exp(-\sigma^2 t^2 / 2) \cos(\gamma_\mu \langle B \rangle t + \phi) + A_{bg} \cos(\gamma_\mu B_{bg} t + \phi). \quad (2)$$

Here $A(0)$ and A_{bg} are the initial asymmetries of the muons hitting and missing the sample respectively. $\langle B \rangle$ and B_{bg} are the internal and background magnetic fields, respectively. ϕ is the initial phase and σ is the Gaussian muon spin relaxation rate of the muon precession signal. The background signal is due to the muons implanted on the outer silver mask where the relaxation rate of the muon precession signal is negligible due to very weak nuclear moments in silver. Fig. 2c shows the temperature dependence of σ and internal field of sample-A. $\sigma(T)$ shows a change in slope at $T = T_c$ which keeps on increasing with further lowering of temperature. Such an increase in $\sigma(T)$ just below T_c indicates that the sample is in the superconducting mixed state and the formation of vortex lattice has created an inhomogeneous field distribution at the muon sites. The internal fields felt by the muons show a diamagnetic shift in the superconducting state of LaPt₃P, a clear signature of bulk superconduc-

tivity in this material.

The true contribution of the vortex lattice field distribution to the relaxation rate σ_{sc} can be estimated as $\sigma_{sc} = (\sigma^2 - \sigma_{nm}^2)^{1/2}$, where $\sigma_{nm} = 0.1459(4) \mu s^{-1}$ is the nuclear magnetic dipolar contribution assumed to be temperature independent. Within the Ginzburg-Landau theory of the vortex state, σ_{sc} is related to the London penetration depth λ of a SC with high upper critical field by the Brandt equation [16]:

$$\frac{\sigma_{sc}(T)}{\gamma_\mu} = 0.06091 \frac{\Phi_0}{\lambda^2(T)}, \quad (3)$$

where $\Phi_0 = 2.068 \times 10^{-15}$ Wb is the flux quantum. The superfluid density $\rho \propto \lambda^{-2}$. Fig. 3 shows the temperature dependence of ρ for LaPt₃P. It clearly varies with temperature down to the lowest temperature 70 mK and shows a linear increase below $T_c/3$. This nonconstant low temperature behaviour is a signature of nodes in the superconducting gap.

The pairing symmetry of LaPt₃P can be understood by analysing the superfluid density data using different models of the gap function $\Delta_{\mathbf{k}}(T)$. For a given pairing model, we compute the superfluid density (ρ) as

$$\rho = 1 + 2 \left\langle \int_{\Delta_{\mathbf{k}}(T)}^{\infty} \frac{E}{\sqrt{E^2 - |\Delta_{\mathbf{k}}(T)|^2}} \frac{\partial f}{\partial E} dE \right\rangle_{FS}. \quad (4)$$

Here, $f = 1 / (1 + e^{\frac{E}{k_B T}})$ is the Fermi function and $\langle \rangle_{FS}$ represents an average over the Fermi surface (assumed to be spherical). We take $\Delta_{\mathbf{k}}(T) = \Delta_m(T)g(\mathbf{k})$ where we assume a universal temperature dependence $\Delta_m(T) = \Delta_m(0) \tanh [1.82 \{1.018 (T_c/T - 1)\}^{0.51}]$ [17] and the function $g(\mathbf{k})$ contains its angular dependence. We use three different pairing models: *s-wave* (single uniform superconducting gap), *p-wave* (two point nodes at the two poles) and *chiral d-wave* (two point nodes at the two poles and a line node at the equator as shown in the inset of Fig. 3). The fitting parameters are given in the Supplemental Material. We note from Fig. 3 that both the *s-wave* and the *p-wave* models lead to saturation in ρ at low temperatures which is clearly not the case for LaPt₃P and the *chiral d-wave* model gives an excellent fit down to the lowest temperature. Nodal SCs are rare since the SC can gain condensation energy by eliminating nodes in the gap. Thus the simultaneous observation of nodal and TRS-breaking superconductivity makes LaPt₃P a unique material.

Discussion

We investigate the normal state properties of LaPt₃P by a detailed band structure calculation using density functional theory within the generalized gradient approximation consistent with previous studies [12, 18]. LaPt₃P is centrosymmetric with a paramagnetic normal state respecting TRS. It has significant effects of spin-orbit

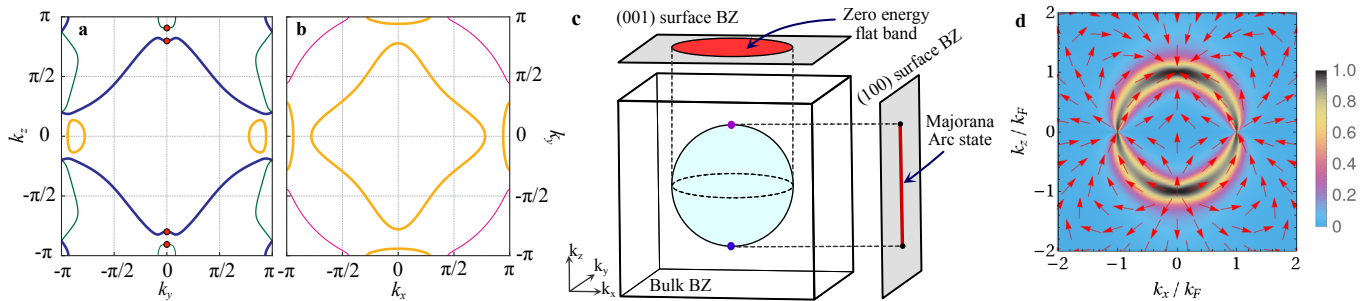


FIG. 4. **Properties of the normal and superconducting states of LaPt₃P.** Projections of the four Fermi surfaces of LaPt₃P with SOC on the $y-z$ plane in **a** and $x-y$ plane in **b**. The thickness of the lines are proportional to the contribution of the Fermi surfaces to the DOS at the Fermi level (green– 10.3%, blue– 43.4%, orange– 40% and magenta– 6.3%). The point nodes of the *chiral d-wave* gap are shown by red dots in **a** and the line node reside on the $x-y$ plane in **b**. **c**) Schematic view of the Majorana Fermi-arc and the zero energy Majorana flat-band corresponding to the two Weyl point nodes and the line node respectively on the respective surface Brillouin zones (BZs) assuming a spherical Fermi surface. **d**) Berry curvature $\mathbf{F}(\mathbf{k})$ corresponding to the two Weyl nodes on the $x-z$ plane. Arrows show the direction of $\mathbf{F}(\mathbf{k})$ and the colour scale shows its magnitude $= \frac{2}{\pi} \arctan(|\mathbf{F}(\mathbf{k})|)$. $\Delta_0 = 0.5\mu$ was chosen for clarity while a more realistic weak-coupling limit $\Delta_0 \ll \mu$ gives a more sharply peaked curvature at the Fermi surface.

coupling (SOC) induced band splitting near the Fermi level (~ 120 meV, most apparent along the MX high symmetry direction). Kramer’s degeneracy survives in the presence of strong SOC due to centrosymmetry and SOC only produces small deformations in the Fermi surfaces [19]. The shapes of the Fermi surfaces play an important role in determining the thermodynamic properties of the material. The projections of the four Fermi surfaces of LaPt₃P on the $y-z$ and $x-y$ plane are shown in Fig. 4a and Fig. 4b respectively with the Fermi surface sheets having the most projected-DOS at the Fermi level shown in blue and orange. It shows the multi-band nature of LaPt₃P with orbital contributions mostly coming from the $5d$ orbitals of Pt and the $3p$ orbitals of P.

LaPt₃P has a nonsymmorphic space group $P4/mmm$ (No. 129) with point group D_{4h} . From the group theoretical classification of the SC order parameters within the Ginzburg-Landau theory [15, 20], the only possible superconducting instabilities with strong SOC which can break TRS spontaneously at T_c correspond to the two 2D irreducible representations, E_g and E_u , of D_{4h} [21]. The superconducting ground state in the E_g channel is a pseudospin *chiral d-wave* singlet state with gap function $\Delta(\mathbf{k}) = \Delta_0 k_z (k_x + ik_y)$ where Δ_0 is an amplitude independent of \mathbf{k} . While the E_u order parameter is a pseudospin *nonunitary chiral p-wave* triplet state with d -vector $\mathbf{d}(\mathbf{k}) = [c_1 k_z, ic_1 k_z, c_2 (k_x + ik_y)]$ where c_1 and c_2 are material dependent real constants independent of \mathbf{k} .

We compute the quasi-particle excitation spectrum for the two TRS breaking states on a generic single band spherical Fermi surface using the Bogoliubov-de Gennes mean field theory [15, 20]. The *chiral d-wave* singlet state leads to an energy gap $= |\Delta_0| |k_z| \sqrt{k_x^2 + k_y^2}$. It has a line node at the “equator” for $k_z = 0$ and

two point nodes at the “north” and “south” poles (shown in Fig. 4a). The low temperature thermodynamic properties are, however, dominated by the line node because of its larger low energy DOS than the point nodes. The triplet state has an energy

gap $= \sqrt{g(k_x, k_y) + 2c_1^2 k_z^2 - 2|c_1| |k_z| \sqrt{f(k_x, k_y) + c_1^2 k_z^2}}$ where $f(k_x, k_y) = c_2^2 (k_x^2 + k_y^2)$. It has only two point nodes at the two poles and no line nodes. Thus, the low temperature linear behaviour of the superfluid density of LaPt₃P shown in Fig. 3 is only possible in the *chiral d-wave* state with a line node in contrast to the triplet state with only point nodes which will give a quadratic behaviour and saturation at low temperatures. Thus LaPt₃P is one of the rare unconventional SCs for which we can unambiguously identify the superconducting order parameter. The point nodes and the line node for the *chiral d-wave* state on the Fermi surface sheets of LaPt₃P are shown in Fig. 4a and Fig. 4b.

We now discuss the topological properties of the *chiral d-wave* state of LaPt₃P based on a generic single-band spherical Fermi surface (chemical potential $\mu = k_F^2 / (2m)$ where k_F is the Fermi wave vector and m is the electron mass) [7, 22]. However, topological protection of the nodes also ensures stability against multiband effects. The effective angular momentum of the Cooper pairs is $L_z = +1$ (in units of \hbar) with respect to the *chiral c*-axis. The equatorial line node acts as a vortex loop in momentum space [23] and is topologically protected by a 1D winding number $w(k_x, k_y) = 1$ for $k_x^2 + k_y^2 < k_F^2$ and $= 0$ otherwise. The nontrivial topology of the line node leads to two-fold degenerate zero-energy Majorana bound states in a flat band on the $(0, 0, 1)$ surface BZ as shown in Fig. 4c. As a result, there is a diverging zero-energy DOS leading to a zero-bias conductance peak (which can be really sharp [24]) measurable in STM. This inversion

symmetry protected line node is extra stable due to even parity SC [3, 24]. The point nodes on the other hand are Weyl nodes and are impossible to gap out by symmetry-preserving perturbations. They act as a monopole and an anti-monopole of Berry flux as shown in Fig. 4d and are characterized by a k_z dependent topological invariant, the sliced Chern number $C(k_z) = L_z$ for $|k_z| < k_F$ with $k_z \neq 0$ and $= 0$ otherwise (see the Supplemental Material for details). As a result, the (1, 0, 0) and (0, 1, 0) surface BZs each have a Majorana Fermi arc which can be probed by STM as shown in Fig. 4c. There are two-fold degenerate chiral surface states with linear dispersion carrying surface currents leading to local magnetisation that may be detectable using SQUID magnetometry. One of the key signatures of chiral edge states is the anomalous thermal Hall effect (ATHE) which depends on the length of the Fermi arc in this case. Impurities in the bulk can, however, increase the ATHE signal by orders of magnitude [25] over the edge contribution making it possible to detect with current experimental technology [26]. We also note that a 90° rotation around the c -axis for the chiral d -wave state leads to a phase shift of $\pi/2$ which can be measured by corner Josephson junctions [27].

Acknowledgments: PKB gratefully acknowledges the ISIS Pulsed Neutron and Muon Source of the UK Science & Technology Facilities Council (STFC) and Paul Scherrer Institut (PSI) in Switzerland for access to the muon beam times. SKG thanks Jorge Quintanilla and Adhip Agarwala for stimulating discussions and acknowledges the Leverhulme Trust for support through the Leverhulme early career fellowship. The work at the University of Warwick was funded by EPSRC, UK, Grant EP/T005963/1. XX is partially supported by the National Natural Science Foundation of China (Grants 11974061, U1732162). NDZ thanks K. Povarov and acknowledges support from the Laboratory for Solid State Physics, ETH Zurich where synthesis studies were initiated.

SUPPLEMENTARY MATERIAL

In this Supplemental Material, we present details of the synthesis, characterization measurements, experimental methods and data analysis of the LaPt₃P samples grown at Warwick, United Kingdom and at ETH, Switzerland. We also give additional band structure results, details of the symmetry analysis and topological properties of the chiral d -wave state of LaPt₃P.

Synthesis and characterization of the sample grown at Warwick, United Kingdom

Polycrystalline LaPt₃P [11] samples (sample-A) were synthesized by a solid state reaction method. Powders of

elemental platinum, red phosphorus, and alkaline earth (lanthanum) were mixed in an argon-filled glove box, and sealed in a quartz tube filled with argon gas. The tube was initially heated to 400 °C and held at this temperature for 12 h in order to avoid rapid volatilization of phosphorus, then reacted at 900 °C for 72 h. The sintered pellet was reground and further annealed at 900 °C within argon-filled quartz tubes for several days and finally quenched into iced water.

The room-temperature structure was determined via powder x-ray diffraction (PXRD). PXRD was measured using a Bruker D5000 general purpose powder diffractometer. The diffraction pattern is shown in Fig. 5. Rietveld refinement was carried out using the TOPAS software package [28] which gave the parameters shown in Table I.

TABLE I. Crystallographic and Rietveld refinement parameters obtained on LaPt₃P.

Space-group	$P4nmm$ (No. 129)				
Formula units/unit cell (Z)	2				
Lattice parameter					
a (Å)	5.7683(6) (at 300K)				
c (Å)	5.4681(7) (at 300K)				
V_{cell} (Å ³)	182.4				
Atom	Wyckoff Position	Occupancy	x	y	z
Pt(1)	4e	1	0.25	0.25	0.5
Pt(2)	2c	1	0	0.5	0.1476(8)
La(1)	2a	1	0	0.5	0.758(4)
P(1)	2c	1	0	0	0

The heat capacity in zero field was measured using a Quantum Design Physical Property Measurement System (PPMS) with a He³ insert to get down to 0.5 K. The total specific heat C_{tot} at low temperatures is made up of several contributions,

$$C_{\text{tot}} = C_{\text{el}} + C_{\text{ph}} + C_{\text{hyp}} \quad (5)$$

where C_{el} is the electronic specific heat having the form in the normal state

$$C_{\text{el}} = \gamma_n T \quad (6)$$

with γ_n being the Sommerfeld coefficient, C_{ph} is the specific heat due to the phonons given by

$$C_{\text{ph}} = \beta_3 T^3 + \beta_5 T^5 \quad (7)$$

with β_3 and β_5 being temperature independent parameters, and C_{hyp} is a contribution due to hyperfine splitting

$$C_{\text{hyp}} \propto 1/T^2. \quad (8)$$

Fitting the normal state specific heat gives $\gamma_n = 9.78(7)$ mJ/mol-K, $\beta_3 = 0.369(14)$ mJ/mol-K⁴ and $\beta_5 =$

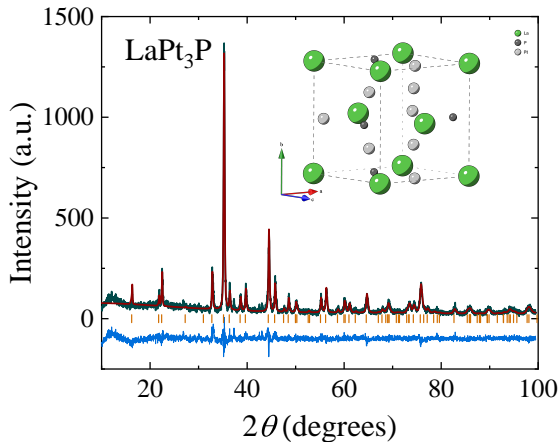


FIG. 5. **Powder x-ray diffraction pattern of the sample-A of LaPt₃P at room temperature.** X-ray diffraction pattern of LaPt₃P at room temperature where the green, red and blue lines indicate the experimental data, the fit and the difference between the data and the fit, respectively. The orange dashes indicate the expected Bragg peaks. The inset shows the structure of a unit cell of LaPt₃P.

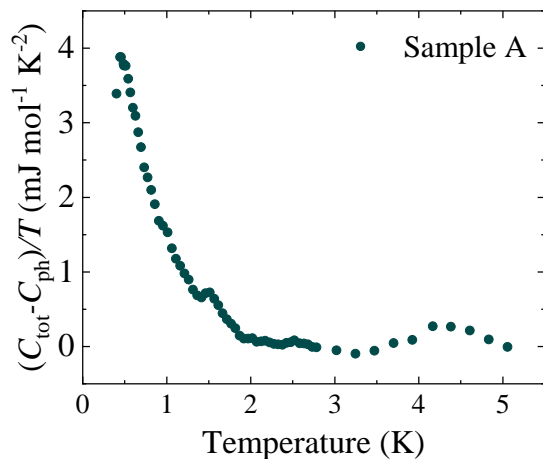


FIG. 6. **Heat capacity of the sample-A of LaPt₃P in zero-field.** $(C_{tot} - C_{ph})/T$ as a function of temperature. There is a small anomaly close to the expected superconducting transition temperature that is masked by a large hyperfine contribution.

$5.47(5) \mu\text{J}/\text{mol}\cdot\text{K}^4$. We then subtract the phonon contribution to the specific heat to plot the electronic specific heat including the hyperfine contribution. This is shown in the Fig. 6 for the sample-A of LaPt₃P, and is consistent with the previous measurement of Ref.[11]. We note that the specific heat has a small anomaly close to the expected $T_c \approx 1.1$ K which is obscured by an upturn at lower temperatures. This is due to a large hyperfine contribution to the specific heat.

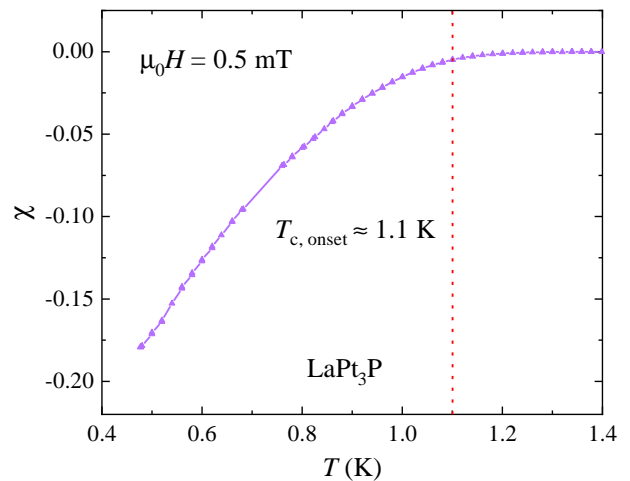


FIG. 7. **Zero-field-cooled magnetic susceptibility of the sample-A of LaPt₃P as a function of temperature.**

The magnetic susceptibility was measured using a Quantum Design Magnetic Property Measurement System (MPMS) using an i-quantum ³He insert. As seen from Fig. 7 this sample has a relatively low Meissner fraction ($\sim 30\%$).

Synthesis and characterization of the sample grown at ETH, Switzerland

A polycrystalline sample of LaPt₃P (sample-B) was synthesized using the cubic anvil high-pressure and high-temperature technique. Starting powders of LaP and Pt of high purity (99.99%) were weighed according to the stoichiometric ratio, thoroughly ground, and enclosed in a boron nitride container, which was placed inside a pyrophyllite cube with a graphite heater. The details of experimental setup can be found in Ref.[29]. All the work related to the sample preparation and the packing of the high pressure cell-assembly was performed in an argon-filled glove box. In a typical run, a pressure of 2 GPa was applied at room temperature. The temperature was ramped in 3 h to the maximum value of 1500 °C, maintained for 5 h, and then cooled to 1350 °C over 5 h and finally reduced to room temperature in 3 h. Afterward, the pressure was released, and the sample was removed. The sample exhibits a large diamagnetic response with the superconducting transition temperature of 1.1 K.

Susceptibility measurements were performed using a Quantum Design Magnetic Property Measurement System (MPMS) by cooling the sample at base temperature in zero field and then apply 7 mT magnetic field. Data were collected while warming up the sample temperature. As shown in the main text, the temperature dependence of the susceptibility data shows a bulk superconducting transition with a T_c at around 1.1 K.

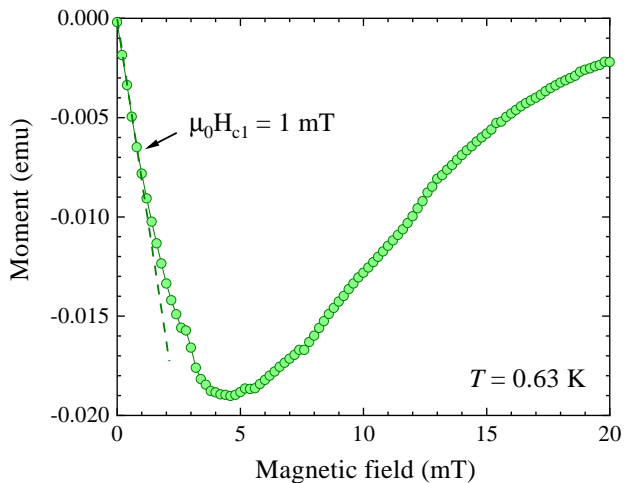


FIG. 8. Magnetic field dependence of the virgin magnetisation curve for sample-B of LaPt_3P . We note that the lower critical field $\mu_0 H_{c1} \approx 1$ mT.

A virgin magnetisation curve was measured at 0.63 K in a Quantum Design MPMS. A linear deviation of the magnetisation curve at low field region (see Fig. 8) shows that the lower critical field H_{c1} of LaPt_3P is around 1 mT.

μSR technique

μSR is a very sensitive local magnetic probe utilizing fully spin-polarized muons [13]. In a μSR experiment polarized muons are implanted into the host sample. After thermalization, each implanted muon decays (lifetime $\tau_\mu = 2.2 \mu\text{s}$) into a positron (and two neutrinos) emitted preferentially in the direction of the muon's spin at the time of decay. Using detectors appropriately positioned around the sample, the decay positrons are detected and time stamped. From the collected histograms, the asymmetry in the positron emission as a function of time, $A(t)$, can be determined, which is directly proportional to the time evolution of the muon spin polarization.

μSR measurements were performed on sample-A in the MUSR spectrometer at the ISIS Pulsed Neutron and Muon Source, UK, and on sample-B in the LTF spectrometer at the Paul Scherrer Institut (PSI), Switzerland. The polycrystalline samples of LaPt_3P in the form of powder were mounted on high purity silver sample holders. The samples were cooled from above T_c to base temperature in zero field for ZF- μSR measurements, and in a field for the TF- μSR measurements. The external field was 10 mT for the TF- μSR measurements performed at ISIS and was 7 mT for the TF- μSR measurements performed at PSI. ZF- μSR measurements were performed in true zero field, achieved by three sets of orthogonal coils working as an active compensation system which cancel

any stray fields at the sample position down to $1.0 \mu\text{T}$. LF- μSR measurements were also performed under similar field-cooled conditions. The typical counting statistics were ~ 40 and ~ 24 million muon decays per data point at ISIS and PSI, respectively. The ZF-, LF- and TF- μSR data were analyzed using the equations given in the text.

The zero temperature upper critical field for LaPt_3P , $\mu_0 H_{c2} \approx 0.12$ T which is much larger than the applied transverse fields in the TF- μSR measurements. The detailed parameters for the analysis of superfluid density data from the TF- μSR measurements for the two samples using the different gap models mentioned in the main text are given in the Table II.

Band structure

LaPt_3P crystallizes in a centrosymmetric primitive tetragonal crystal structure. The corresponding space group is $P4/nmm$ (No. 129) which is nonsymmorphic. The point group of the Bravais lattice is D_{4h} . The nonsymmorphic symmetries within a unit cell include both screw axes and glide planes. We have performed detailed band structure calculations of LaPt_3P using density functional theory (DFT). The corresponding band structure results with and without spin orbit coupling (SOC) are shown in Fig. 9(a) and Fig. 9(b) respectively. We note that this material has significant splitting of bands due to SOC [18]. The maximum band splitting caused by the SOC near the Fermi level is estimated to be ~ 120 meV and is most apparent along the MX high symmetry direction. The SOC induced band splitting breaks the spin-symmetry and have important consequences in Cooper-pairing in this material.

The 3D Fermi surfaces were plotted by the XCrySDen packages [30]. The Fermi surfaces with SOC are shown in Fig. 10. We note that there are four Fermi surfaces with the middle two shown in Fig. 10(b) and Fig. 10(c); and again in Fig. 10(f) and Fig. 10(g) from a different view, contributing the most to the density of states (DOS) at the Fermi level. This is seen from the projected DOS at the Fermi level shown in Fig. 11. Fig. 11(a) shows the contributions of the different atomic orbitals to the DOS at the Fermi level. We note that Pt-5d orbitals contribute the most. Thus LaPt_3P is a multi-band system. Fig. 11(a) shows the contributions of the different Fermi surfaces to the DOS at the Fermi level.

Symmetry analysis

In this section we describe, the symmetry analysis of the possible superconducting order parameters for LaPt_3P . To proceed, we note the properties of the material: it is centrosymmetric, has nonsymmorphic symmetries, has considerable effects of SOC, has multiple

TABLE II. Summary of the analysis of the superfluid density data for the two samples of LaPt₃P.

Model	$g(\theta, \phi)$	Gap type	Reduced least-squared deviation (χ_r^2)	Fitted $\Delta_m(0)/(k_B T_c)$
<i>s</i> -wave	1	nodeless	13.025	1.270 ± 0.020
<i>p</i> -wave	$\sin(\theta)e^{i\phi}$	two point nodes	4.537	1.693 ± 0.029
chiral <i>d</i> -wave	$\sin(2\theta)e^{i\phi}$	two point nodes + a line node	2.238	1.989 ± 0.011

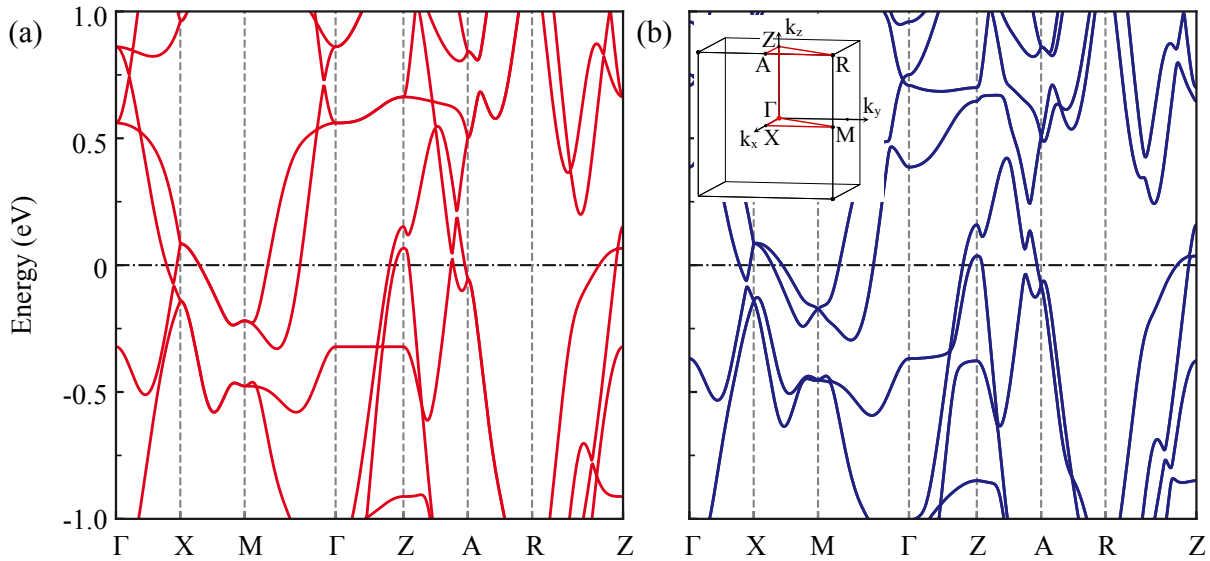


FIG. 9. **First principles band structure results of LaPt₃P.** a) Band structure without SOC. b) Band structure with SOC. The primitive tetragonal Brillouin zone with the marked high symmetry points and directions used in the band structure computation is shown in the inset of (b). We note that SOC induces significant band splitting near the Fermi level especially from M to X.

bands potentially participating in superconductivity, has spontaneously broken TRS at T_c and has line nodes dominating its thermodynamic behavior.

The normal state symmetry group of the system is given by $\mathcal{G} = G_0 \otimes U(1) \otimes \mathcal{T}$, where $U(1)$ is the gauge symmetry group, G_0 is the group of symmetries containing the point group symmetries of D_{4h} and spin rotation symmetries in 3D of $SO(3)$ and \mathcal{T} is the group of time-reversal symmetry (TRS). The Ginzburg-Landau (GL) free energy of the system must be invariant under this symmetry group.

The D_{4h} point group has 8 one-dimensional irreducible representations (irreps) (4 of them have even parity and the other 4 have odd parity) and 2 two dimensional irreps (one with even parity denoted by E_g and the other with odd parity denoted by E_u). Centrosymmetry implies that this material has either purely triplet or purely singlet superconducting instability in general. Furthermore, a TRS breaking superconducting order parameter requires degenerate or multi-dimensional irreps. This system can thus lead to such type of instability only in the E_g or the E_u irrep. We will now focus only on these

two irreps and construct possible superconducting order parameters for the system. We consider strong SOC as uncovered by the band structure calculation of this material.

The fourth order invariant corresponding to the 2 two-dimensional irreps E_g and E_u of D_{4h} gives the quartic order term of the GL free energy [20, 31] to be

$$f_4 = \beta_1(|\eta_1|^2 + |\eta_2|^2)^2 + \beta_2|\eta_1^2 + \eta_2^2|^2 + \beta_3(|\eta_1|^4 + |\eta_2|^4) \quad (9)$$

where (η_1, η_2) are the two complex components of the two-dimensional order parameters. This free energy needs to be minimized with respect to both η_1 and η_2 . The nonequivalent solutions are: $(\eta_1, \eta_2) = (1, 0)$, $\frac{1}{\sqrt{2}}(1, 1)$ and $\frac{1}{\sqrt{2}}(1, i)$. There is an extended region in the parameter space where the states corresponding to $(\eta_1, \eta_2) = (1, i)$ is stabilized. The instabilities corresponding to this case spontaneously break TRS at T_c due to a nontrivial phase difference between the two order parameter components.

Then the even parity superconducting order parameter

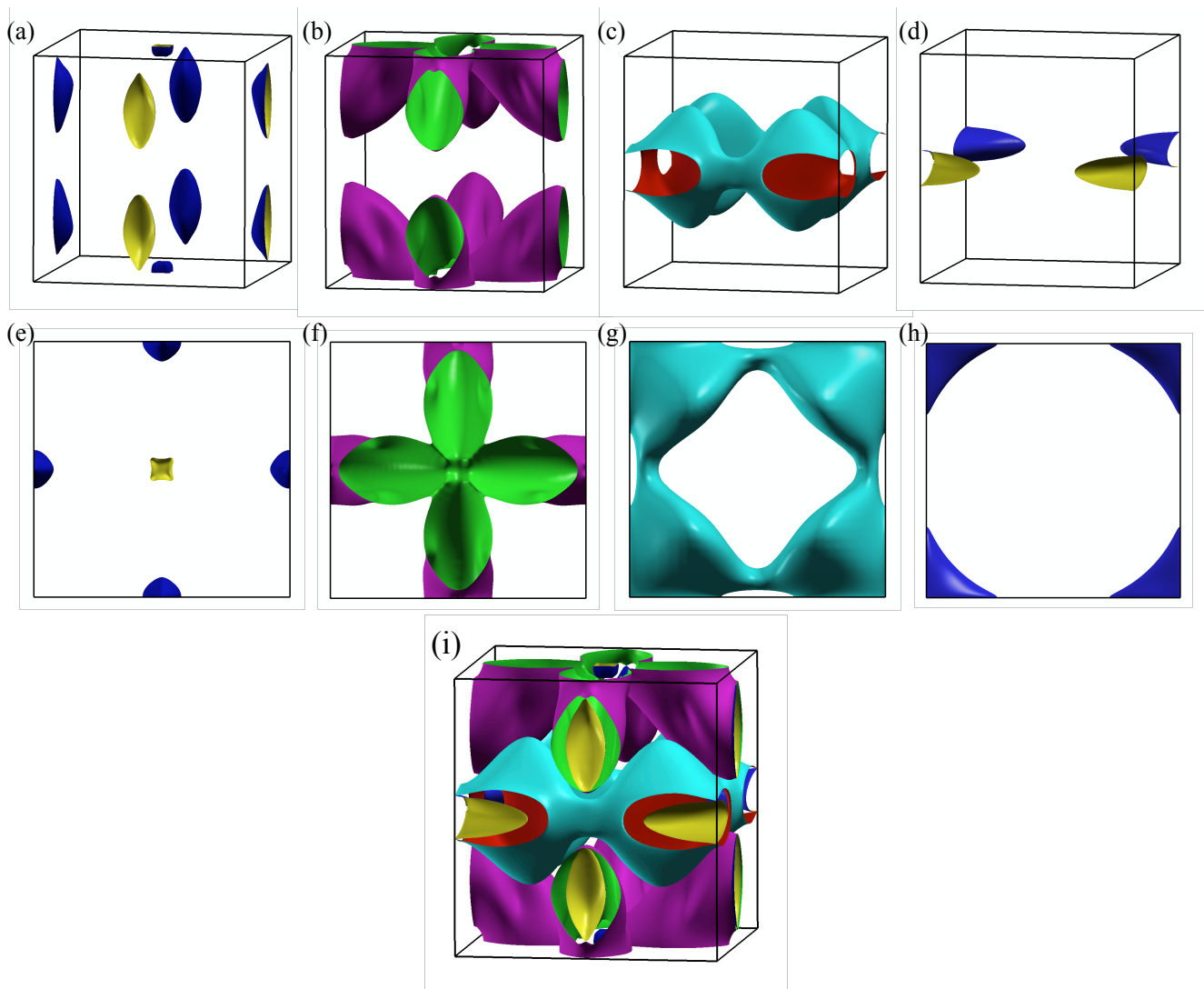


FIG. 10. **Fermi surfaces of LaPt₃P with SOC.** Panels (a)–(d) are from a side view and the panels (e)–(h) are from the top view for the four Fermi surface sheets and (i) shows a combined Fermi surface.

belonging to E_g is given by

$$\Delta(\mathbf{k}) = \Delta_0 k_z (k_x + ik_y) \quad (10)$$

where Δ_0 is the real amplitude independent of \mathbf{k} . This is a *chiral d-wave* singlet order parameter. The odd parity superconducting order parameter belonging to E_u gives rise to the gap matrix $\hat{\Delta}(\mathbf{k}) = [\mathbf{d}(\mathbf{k}) \cdot \vec{\sigma}] i\sigma_y$ where $\vec{\sigma}$ denotes the three Pauli spin matrices and $\mathbf{d}(\mathbf{k})$ is the triplet d -vector given by

$$\mathbf{d}(\mathbf{k}) = [Ak_z, iAk_z, B(k_x + ik_y)]. \quad (11)$$

Here, A and B are material dependent real constants independent of \mathbf{k} and in general they are nonzero. We note that the values of A and B determine the orientation of the d -vector. For example, for $A = 0$ the d -vector points along the c -axis and for $B = 0$ the d -vector points

in the ab -plane. We also note that

$$\mathbf{d}(\mathbf{k}) \times \mathbf{d}^*(\mathbf{k}) = 2iAk_z (Bk_x \hat{x} - Bk_y \hat{y} - Ak_z \hat{z}) \quad (12)$$

which is nonzero in general. Hence, this superconducting state is *nonunitary chiral p-wave* triplet state.

The strong SOC case considered here implies that the single particle states are no longer the eigenstates of spin and we need to label them rather by pseudospins. The pseudospin states are linear combinations of the spin eigenstates. Since the pseudospin and the spin are closely related, the even parity states correspond to pseudospin singlet and the odd parity states correspond to pseudospin triplet states.

We can now follow the standard Bogoliubov-de Gennes mean field theory [20] to compute the quasi-particle excitation energy spectrum for the two TRS breaking states given in Eqn. (10) and Eqn. (11). The schematic view of

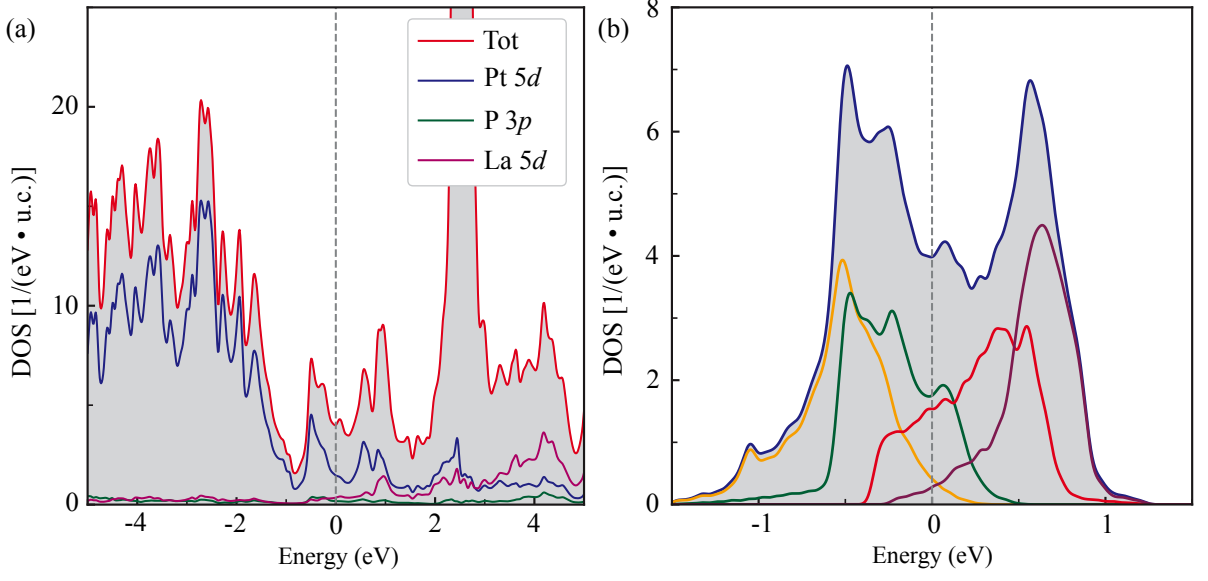


FIG. 11. **Projected density of states (DOS) results.** Left panel shows the contributions of different orbitals to the DOS. We note that Pt 5d orbitals contribute the most to the DOS at the Fermi level. The right panel shows the DOS contributions of the different Fermi surfaces. The blue is total and the other four correspond to the four Fermi surfaces. Their contributions at the Fermi level are 10.3%, 43.4%, 39.5% and 6.3%.

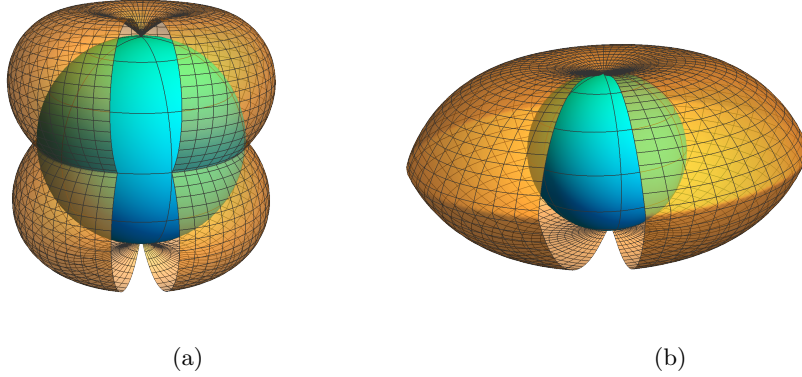


FIG. 12. **Polar plots of the excitation energy gaps.** (a) The chiral d -wave singlet case and (b) the nonunitary chiral p -wave triplet case. In both the cases, point nodes appear at the two “poles”, while the singlet case has an additional line node at the “equator”.

the excitation energy gaps for the two order parameters are shown in Fig. 12.

with Δ_0 being the pairing amplitude, we assume a simplified single band parabolic dispersion (in units of \hbar)

$$\xi(\mathbf{k}) = \frac{k^2}{2m} - \mu, \quad (14)$$

Topological properties of the chiral singlet state

To discuss the topological properties of the nodal excitations for the chiral d -wave state with the gap function

$$\Delta(\mathbf{k}) = \frac{\Delta_0}{k_F^2} k_z (k_x + ik_y) \quad (13)$$

where m is the mass of an electron, $\mu = \frac{k_F^2}{2m}$ is the chemical potential and k_F is the Fermi wavevector. We note that $\Delta(\mathbf{k}) \sim Y_1^2(\theta, \phi)$ where $Y_m^l(\theta, \phi)$ are the spherical harmonics. Thus the Cooper pairs have an angular momentum $L_z = +1$ for this state.

Then Bogoliubov-de Gennes Hamiltonian in the pseu-

dospin basis can be written as

$$\mathcal{H} = \sum_{\mathbf{k}} \Psi_{\mathbf{k}}^\dagger H(\mathbf{k}) \Psi_{\mathbf{k}} \quad (15)$$

where $\Psi_{\mathbf{k}} = (c_{\mathbf{k}\uparrow}, c_{-\mathbf{k}\uparrow}^\dagger)^T$ with $c_{\mathbf{k}\sigma}$ being the fermion annihilation operator with pseudospin flavor $\sigma \in \{\uparrow, \downarrow\}$. We can rewrite the BdG Hamiltonian as

$$H(\mathbf{k}) = \mathbf{N}(\mathbf{k}) \cdot \boldsymbol{\tau} \quad (16)$$

where $\boldsymbol{\tau}$ is the vector of the three Pauli matrices in the particle-hole space and $\mathbf{N}(\mathbf{k}) = \left\{ \frac{\Delta_0}{k_F^2} k_z k_x, \frac{\Delta_0}{k_F^2} k_z k_y, \xi(\mathbf{k}) \right\}$ is a pseudospin vector. The eigenvalues of the Hamiltonian in Eqn. (16) are $\pm E(\mathbf{k})$ where

$$E(\mathbf{k}) = |\mathbf{N}(\mathbf{k})| = \sqrt{\xi^2(\mathbf{k}) + |\Delta(\mathbf{k})|^2}. \quad (17)$$

Hence, the superconducting ground state has two point nodes at the two poles of the Fermi surface $\mathbf{k}_\pm = (0, 0, \pm k_F)$ and a line node at the equator $k_z = 0$ plane. The low energy Hamiltonian close to two point nodes can be written as

$$H(\mathbf{k}) = \frac{\Delta_0}{k_F} (p_x \tau_x - p_y \tau_y) \pm v_F p_z \tau_z \quad (18)$$

where we have defined $\mathbf{p} = (\mathbf{k} - \mathbf{k}_\pm)$. This is a Weyl Hamiltonian. Thus the two point nodes are also Weyl nodes. As a result they are impossible to gap out since there is no fourth Pauli matrix which can come from a mass term to gap out the nodes.

The corresponding Bloch wave functions $|u_\pm(\mathbf{k})\rangle$ are the eigenfunctions of $\hat{\mathbf{n}}(\mathbf{k}) \cdot \boldsymbol{\sigma}$ with eigenvalues ± 1 where $\hat{\mathbf{n}}(\mathbf{k}) = \mathbf{N}(\mathbf{k})/|\mathbf{N}(\mathbf{k})|$ is the unit vector along the direction of the pseudospin $\mathbf{N}(\mathbf{k})$. We note that this unit vector $\hat{\mathbf{n}}(\mathbf{k})$ is well defined only when $|\mathbf{N}(\mathbf{k})| \neq 0$ i.e. in the nodeless regions on the Fermi surface. In spherical coordinates, parametrizing $\hat{\mathbf{n}}(\mathbf{k}) = [n_x(\mathbf{k}), n_y(\mathbf{k}), n_z(\mathbf{k})] = [\sin(\theta) \cos(\phi), \sin(\theta) \sin(\phi), \cos(\theta)]$ we have

$$|u_-(\mathbf{k})\rangle = \begin{bmatrix} \cos(\frac{\theta}{2}) e^{-i\phi} \\ \sin(\frac{\theta}{2}) \end{bmatrix} \text{ and } |u_+(\mathbf{k})\rangle = \begin{bmatrix} \sin(\frac{\theta}{2}) e^{-i\phi} \\ -\cos(\frac{\theta}{2}) \end{bmatrix}. \quad (19)$$

Then from the negative energy occupied states $|u_-(\mathbf{k})\rangle$ the Berry connection is defined as

$$\mathbf{A}(\mathbf{k}) = i \langle u_-(\mathbf{k}) | \nabla_{\mathbf{k}} | u_-(\mathbf{k}) \rangle \quad (20)$$

and the corresponding Berry curvature is $\mathbf{F}(\mathbf{k}) = \nabla_{\mathbf{k}} \times \mathbf{A}(\mathbf{k})$. In terms of the components of $\hat{\mathbf{n}}(\mathbf{k})$, it is given by $\mathbf{F}(\mathbf{k}) = [n_y(\mathbf{k}) \{ \nabla_{\mathbf{k}} n_z(\mathbf{k}) \times \nabla_{\mathbf{k}} n_x(\mathbf{k}) \} - n_x(\mathbf{k}) \{ \nabla_{\mathbf{k}} n_z(\mathbf{k}) \times \nabla_{\mathbf{k}} n_y(\mathbf{k}) \}] / [2 \{ n_x^2(\mathbf{k}) + n_y^2(\mathbf{k}) \}]$.

For the chiral d -wave case, $F_x(\mathbf{k})$ and $F_y(\mathbf{k})$ are odd functions of (k_y, k_z) and (k_x, k_z) respectively. Hence, there is no Berry flux along the x and y directions. The number of field lines coming in and out of the ca and cb planes are the same. Whereas $F_z(\mathbf{k})$ is an even function

of (k_x, k_y) and the flux through the ab plane as a function of k_z is

$$\Phi(\mathbf{k}) = \int dk_x dk_y F_z(\mathbf{k}) = 2\pi \mathcal{C}(k_z). \quad (21)$$

$\mathcal{C}(k_z)$ is the "sliced" Chern number (momentum dependent) of the effective 2D problem for a fixed k_z . For a given value of $|k_z| < k_F$, the Hamiltonian in Eqn. (16) describes an effective 2D problem with fully gapped weak coupling BCS pairing and an effective chemical potential $\frac{\hbar^2}{2m}(k_F^2 - k_z^2)$ having the Chern number $\mathcal{C}(k_z) = +1$. For $|k_z| > k_F$, the effective chemical potential is negative and describes a topologically trivial BEC state. Thus, the Weyl point nodes at $(0, 0, \pm k_F)$ act as monopoles and anti-monopoles of the Berry curvature and the flux through a sphere surrounding the monopole is 2π and that through the anti-monopole is -2π . The topologically protected Weyl nodes give rise to Majorana arc surface states on the surface Brillouin zone corresponding to the $(1, 0, 0)$ and $(0, 1, 0)$ surfaces having chiral linear dispersions along y and x directions respectively. As a result of the arc surface states the system shows anomalous thermal and spin Hall effects [4, 7, 22].

The equatorial line node is characterized by a 1D winding number. This can be defined in terms of the following spectral symmetry [4, 22] of the Hamiltonian. We note that the operator

$$\Gamma_{\mathbf{k}} = \sin(\phi_{\mathbf{k}}) \tau_x + \cos(\phi_{\mathbf{k}}) \tau_y \quad (22)$$

where $\tan(\phi_{\mathbf{k}}) = k_y/k_x$ anticommutes with the Hamiltonian

$$\{H(\mathbf{k}), \Gamma_{\mathbf{k}}\} = 0. \quad (23)$$

As a result any eigenstate of the Hamiltonian $H(\mathbf{k})$ with the eigenvalue $E_{\mathbf{k}}$ is also an eigenstate of the operator $\Gamma_{\mathbf{k}}$ with the eigenvalue $-E_{\mathbf{k}}$. Then with the help of this spectral symmetry $\Gamma_{\mathbf{k}}$ we define the winding number as

$$w(\mathbf{k}_\perp) = -\frac{1}{4\pi i} \oint_{\mathcal{L}} dl \text{Tr} [\Gamma_{\mathbf{k}} H^{-1}(\mathbf{k}) \partial_l H(\mathbf{k})], \quad (24)$$

where dl is the line element along a closed loop \mathcal{L} encircling the line node and $\mathbf{k}_\perp = (k_x, k_y)$. For this case then we have

$$w(\mathbf{k}_\perp) = 1 \quad \forall k_\perp < k_F \quad (25)$$

$$= 0 \quad \text{otherwise.} \quad (26)$$

We note that the winding number does not depend on the angular momentum of the Cooper pairs. This non-trivial topology of the line node ensures the existence of zero-energy surface Andreev bound states on the $(0, 0, 1)$ surface. They produce an image of the Fermi surface equator in the corresponding surface Brillouin zone. Being dispersionless, these zero-energy states result in a divergent density of states, and are predicted to give rise

to a zero bias peak in tunneling measurements. These zero modes are two fold degenerate Majorana fermions arising from the twofold spin degeneracy of the pairing interaction.

* pabitra.biswas@stfc.ac.uk

† S.Ghosh@kent.ac.uk

- [1] M. Sato and Y. Ando, “Topological superconductors: a review,” *Reports on Progress in Physics* **80**, 076501 (2017).
- [2] C. Kallin and J. Berlinsky, “Chiral superconductors,” *Reports on Progress in Physics* **79**, 054502 (2016).
- [3] S. Kobayashi, K. Shiozaki, Y. Tanaka, and M. Sato, “Topological Blount’s theorem of odd-parity superconductors,” *Physical Review B* **90**, 024516 (2014).
- [4] P. Goswami and A. H. Nevidomskyy, “Topological Weyl superconductor to diffusive thermal Hall metal crossover in the B-phase of UPt_3 ,” *Physical Review B* **92**, 214504 (2015).
- [5] M. Tinkham, *Introduction to Superconductivity* (McGraw-Hill Inc., 1996).
- [6] D. J. Scalapino, “A common thread: The pairing interaction for unconventional superconductors,” *Reviews of Modern Physics* **84**, 1383 (2012).
- [7] A. P. Schnyder and P. M. R. Brydon, “Topological surface states in nodal superconductors,” *Journal of Physics: Condensed Matter* **27**, 243201 (2015).
- [8] L. Jiao, S. Howard, S. Ran, Z. Wang, J. O. Rodriguez, M. Sigrist, Z. Wang, N. P. Butch, and V. Madhavan, “Chiral superconductivity in heavy-fermion metal UTe_2 ,” *Nature* **579**, 523–527 (2020).
- [9] J. A. Mydosh and P. M. Oppeneer, “Colloquium: Hidden order, superconductivity, and magnetism: The unsolved case of URu_2Si_2 ,” *Reviews of Modern Physics* **83**, 1301–1322 (2011).
- [10] P. K. Biswas, H. Luetkens, T. Neupert, T. Stürzer, C. Baines, G. Pascua, A. P. Schnyder, M. H. Fischer, J. Goryo, M. R. Lees, *et al.*, “Evidence for superconductivity with broken time-reversal symmetry in locally non-centrosymmetric SrPtAs ,” *Physical Review B* **87**, 180503 (2013).
- [11] T. Takayama, K. Kuwano, D. Hirai, Y. Katsura, A. Yamamoto, and H. Takagi, “Strong coupling superconductivity at 8.4 K in an antiperovskite phosphide SrPt_3P ,” *Physical Review Letters* **108**, 237001 (2012).
- [12] A. Subedi, L. Ortenzi, and L. Boeri, “Electron-phonon superconductivity in APt_3P ($A = \text{Sr}, \text{Ca}, \text{La}$) compounds: From weak to strong coupling,” *Physical Review B* **87**, 144504 (2013).
- [13] A. Yaouanc and P. D. De Reotier, *Muon spin rotation, relaxation, and resonance: applications to condensed matter*, Vol. 147 (Oxford University Press, 2011).
- [14] R. S. Hayano, Y. J. Uemura, J. Imazato, N. Nishida, K. Nagamine, T. Yamazaki, Y. Ishikawa, and H. Yasuoka, “Spin fluctuations of itinerant electrons in MnSi studied by muon spin rotation and relaxation,” *Journal of the Physical Society of Japan* **49**, 1773–1783 (1980).
- [15] S. K. Ghosh, M. Smidman, T. Shang, J. F. Annett, A. D. Hillier, J. Quintanilla, and H. Yuan, “Recent progress on superconductors with time-reversal symmetry breaking,” *Journal of Physics: Condensed Matter* **33**, 033001 (2020).
- [16] E. H. Brandt, “Properties of the ideal Ginzburg-Landau vortex lattice,” *Physical Review B* **68**, 054506 (2003).
- [17] A. Carrington and F. Manzano, “Magnetic penetration depth of MgB_2 ,” *Physica C: Superconductivity* **385**, 205–214 (2003).
- [18] H. Chen, X. Xu, C. Cao, and J. Dai, “First-principles calculations of the electronic and phonon properties of APt_3P ($A = \text{Ca}, \text{Sr}, \text{and La}$): Evidence for a charge-density-wave instability and a soft phonon,” *Physical Review B* **86**, 125116 (2012).
- [19] S. Yip, “Noncentrosymmetric superconductors,” *Annu. Rev. Condens. Matter Phys.* **5**, 15–33 (2014).
- [20] M. Sigrist and K. Ueda, “Phenomenological theory of unconventional superconductivity,” *Reviews of Modern Physics* **63**, 239 (1991).
- [21] Nonsymmorphic symmetries can give rise to additional symmetry-required nodes (other than the point group symmetry-required ones) on the Brillouin zone boundaries along the high symmetry directions. The nonsymmorphic symmetries of LaPt_3P , however, can only generate additional point nodes for the E_g order parameter but no additional nodes for the E_u case [32].
- [22] P. Goswami and L. Balicas, “Topological properties of possible Weyl superconducting states of URu_2Si_2 ,” arXiv preprint arXiv:1312.3632 (2013).
- [23] T. T. Heikkilä, N. B. Kopnin, and G. E. Volovik, “Flat bands in topological media,” *JETP Letters* **94**, 233 (2011).
- [24] S. Kobayashi, Y. Tanaka, and M. Sato, “Fragile surface zero-energy flat bands in three-dimensional chiral superconductors,” *Physical Review B* **92**, 214514 (2015).
- [25] V. Ngampruetikorn and J. A. Sauls, “Impurity-induced anomalous thermal Hall effect in chiral superconductors,” *Physical Review Letters* **124**, 157002 (2020).
- [26] M. Hirschberger, R. Chisnell, Y. S. Lee, and N. P. Ong, “Thermal Hall effect of spin excitations in a kagome magnet,” *Physical Review Letters* **115**, 106603 (2015).
- [27] J. D. Strand, D. J. Van Harlingen, J. B. Kycia, and W. P. Halperin, “Evidence for complex superconducting order parameter symmetry in the low-temperature phase of UPt_3 from Josephson interferometry,” *Physical Review Letters* **103**, 197002 (2009).
- [28] A. A. Coelho, “*TOPAS* and *TOPAS-Academic*: an optimization program integrating computer algebra and crystallographic objects written in C++,” *Journal of Applied Crystallography* **51**, 210–218 (2018).
- [29] N. D. Zhigadlo, “High pressure crystal growth of the antiperovskite centrosymmetric superconductor SrPt_3P ,” *Journal of Crystal Growth* **455**, 94 – 98 (2016).
- [30] A. Kokalj, “Computer graphics and graphical user interfaces as tools in simulations of matter at the atomic scale,” *Computational Materials Science* **28**, 155–168 (2003).
- [31] J. F. Annett, “Symmetry of the order parameter for high-temperature superconductivity,” *Adv. Phys.* **39**, 83–126 (1990).
- [32] S. Sumita and Y. Yanase, “Unconventional superconducting gap structure protected by space group symmetry,” *Physical Review B* **97**, 134512 (2018).